Article

Supramolecular assembly guided by photolytic redox cycling

Patrick Roth[1,2], Raphael Meyer[1,2], Iain Harley [ID][1], Katharina Landfester[1], Ingo Lieberwirth[1], Manfred Wagner[1], David Y. W. Ng [ID][1]✉ & Tanja Weil [ID][1]✉

In living systems, the formation of structures relies on balancing kinetic and thermodynamic influences powered by reversible covalent bond chemistry. Although synthetic efforts have replicated these processes to some extent, elucidating their combination is necessary to identify mechanisms that confer nature's structural precision and flexibility within a complex environment. Here we design a photolytic reaction cascade where competing redox pathways control the transience, interconversion and production rates of thiol/disulfide supramolecular monomers in situ. In contrast to direct assembly by dissolution, cascade generation of the same monomers formed hierarchical assemblies with different structural order. Redox-induced cycling between thiol–disulfide formation led to the emergence of new secondary structures and chirality within the final assemblies. These multiple structural states found within the same molecular system demonstrate the concept of assembly plasticity engaged frequently in biology. We demonstrate the importance of reaction complexity in controlling supramolecular propagation and in expanding the library of nanoarchitectures that can be created.

Hierarchical structures in biology are driven by complex reaction pathways with corrective mechanisms to ensure their precision and function within the often-crowded living system. In cells, the number of reactive intermediates and partners engaged in the propagation of a single superstructure far exceeds that of synthetic supramolecular systems, often raising the question of whether such complexity is necessary from a structural perspective. The microtubule of the cytoskeleton, for example, is made up of simple tandem repeats of α- and β-tubulin proteins but involves chemical reactions by seven groups of post-translational modification[1] and a proteome of >500 microtubule-associated proteins that collectively regulate its structure[2,3]. At first glance, the effort to build the microtubule seems to be excessive but recent findings in synthetic systems have found that supramolecular assembly processes are highly delicate[4–9]. Seemingly minimal (<0.01%) changes in liquid–liquid interfaces and composition and in fluid dynamics are as important in directing structure formation as well-established aspects such as concentration, temperature, molecular design and solvent polarity[10–12]. Given that the former set of

factors are dynamic and heterogeneous within the cells, the magnitude and variety of control mechanisms necessary to guide structure formation in cells appear more reasonable.

Within the crowded cellular environment, the production of assembly precursors and their quantity are tightly regulated by interconnected reaction pathways. In this way, the reaction kinetics are coupled to the assembly landscape where the local chemical state and concentration influence the probability of metastable or kinetically trapped structures[13]. The importance of chemical reaction kinetics in controlling supramolecular assemblies has since been demonstrated in synthetic dissipative systems where advances in mimicking cellular homeostasis have showed recent success[14–23]. However, unlike synthetic analogues, biological precursors also modulate polymerization dynamics through structural plasticity, which reflects changes in the structural state without altering its chemical identity[24]. In microtubules, α-/β-tubulin at the polymerization terminal or the receding end are chemically identical yet they create opposite effects upon the global structure. Separate pathways then control the immediate
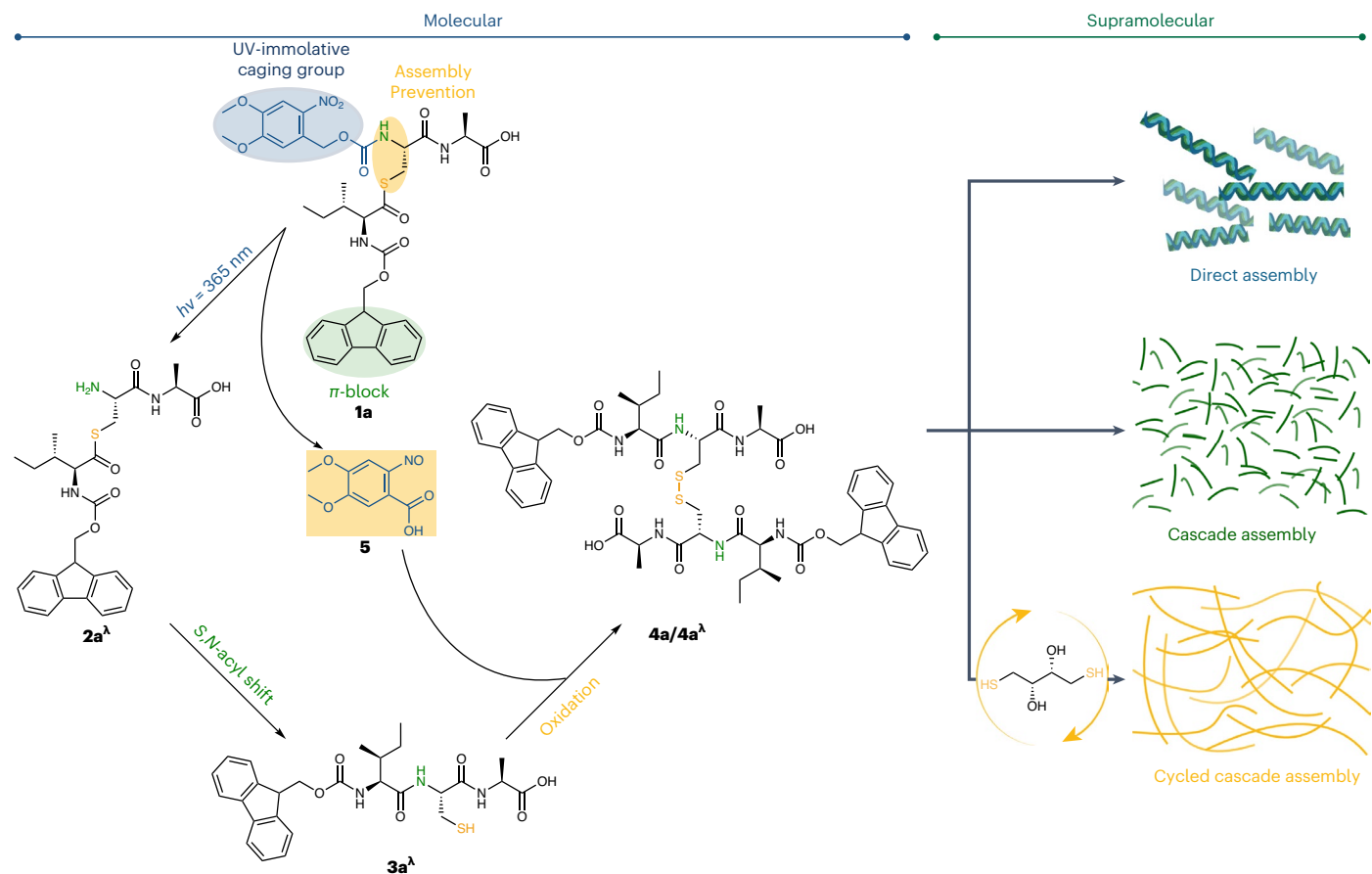
Fig. 1 | Photolytic cascade generation of molecular components and its effect on the formation of different supramolecular nanostructures. The molecular section describes a series of covalent reactions, the combined kinetics of which determine how the assembly precursor is produced in solution. By exposing the precursors to different combinations of reactions, the supramolecular pathway is altered, producing several morphologies despite having the same chemical identity. The reaction pathway of **1a** after ultraviolet irradiation leads to the decaged isopeptide **2a$^\lambda$**, and rearrangement/linearization and oxidation of the thiol **3a$^\lambda$** to the disulfide **4a$^\lambda$**. The nvoc side product **5** enters the cycle as the oxidant to fuel the final step. The addition of DTT reverses the oxidation, causing **3a$^\lambda$** and **4a$^\lambda$** to rapidly interconvert, thereby delaying the production of **4a$^\lambda$**. Depending on the assembly pathway (direct, cascade, cycled cascade) of **4a/4a$^\lambda$**, different supramolecular nanostructures and chirality are produced.
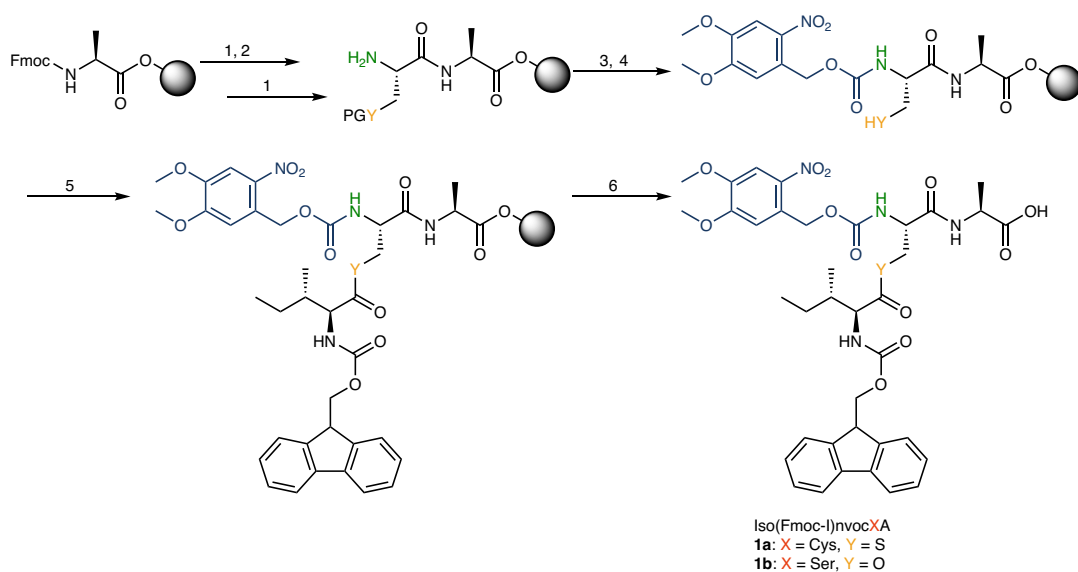

Fig. 2 | Solid-phase synthesis of the isopeptide derivatives. Synthesis of iso(Fmoc-I)nvocXA by solid-phase peptide synthesis: (1) piperidine; (2) Fmoc-X(protecting group)-OH, DIC, ethyl cyanohydroxyiminoacetate (oxyma); (3) 6-nitroveratryl chloroformate (nvoc-Cl), triethylamine; (4) dichloromethane, TIPS, TFA; (5) Fmoc-Ile-OH, DIC, 4-dimethylaminopyridine; (6) TFA, TIPS, H_2O.
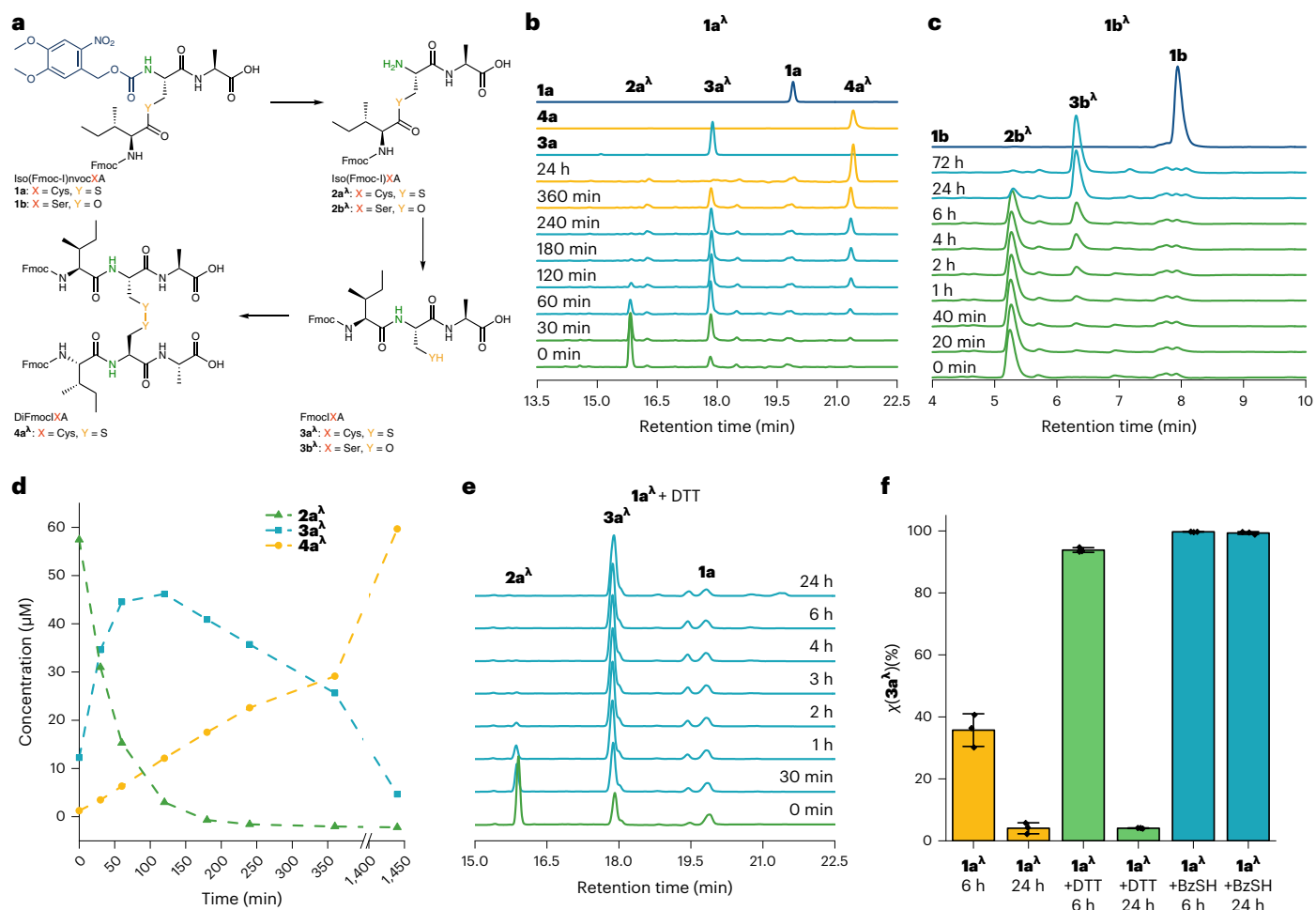
Fig. 3 | Kinetic profile of iso(Fmoc-I)nvocXA derivatives showing accelerated conversion for 1a and recycling pathway. a, Reaction pathway of the two isopeptides after irradiation. **b**, HPLC kinetics of iso(Fmoc-I)nvocCA **1a** in methanol:NH₄HCO₃ buffer (1:1) over the 24 h after irradiation. After deprotection, iso(Fmoc-I)CA **2a**$^\lambda$ rearranges into the linear peptide Fmoc-ICA **3a**$^\lambda$ and oxidizes into the dimer DiFmoc-ICA **4a**$^\lambda$. **c**, HPLC kinetics of iso(Fmoc-I)nvocSA **1b** in methanol:NH₄HCO₃ buffer (1:1) over the 72 h after irradiation. After deprotection, iso(Fmoc-I)SA **2b**$^\lambda$ rearranges into the linear peptide Fmoc-ISA **3b**$^\lambda$. **d**, Concentrations of the intermediates and the product over time (**1a**$^\lambda$) calculated from the calibration curves of **3a** and **4a**. The intermediate **2a**$^\lambda$ was calibrated with **3a**. **e**, HPLC kinetics of iso(Fmoc-I)nvocCA **1a** 100 μM irradiated with DTT 10 mM in methanol:NH₄HCO₃ buffer (1:1). **f**, Molar proportion (χ) of **3a**$^\lambda$ versus **4a**$^\lambda$ after 6 h and 24 h for **1a**$^\lambda$, **1a**$^\lambda$ + 10 equiv. of DTT and **1a**$^\lambda$ + 10 equiv. of benzyl mercaptan. Data are presented as ±s.d., $n = 3$.

environments surrounding the terminals where the cell can regulate the level of order/disorder within the superstructure. By creating additional nodes of complexity in reaction networks, biology gains access to another dimension of supramolecular features.

Inspired by this concept, we first establish a light-promoted molecular transformation cascade that organizes reversible and non-reversible covalent reactions to generate assembly precursors. The reaction kinetics will therefore dictate the availability of precursors over time while the reversible segment will modulate the lifetime of the precursors switching between active states. By controlling these parameters in the reaction cascade, we aim to demonstrate that assembly precursors can access different superstructures that are unavailable via conventional, direct supramolecular assembly.

As the first activator of the reaction cascade, we take the photo-protecting group (PPG) 2-nitroveratryloxycarbonyl (nvoc), for which the mechanism of photolysis and broad substrate capacity are well established[25]. The nvoc group absorbs ultraviolet light (365 nm) to form a zwitterionic excited state followed by an N=O$_{nitro}$ bond scission and the expulsion of CO_2 (ref. 25). The resultant aromatic N=O$_{nitroso}$ group can oxidize thiols into disulfides via sequential addition and elimination steps[26]. By combining both reactions, we propose that

thiol-containing molecules protected with the nvoc group would undergo a self-promoted transformation into disulfides in situ. As the thiol component, we design iso(Fmoc-I)nvocCA **1a**, consisting of a masked cysteine connected via a thioester to form an isomerized backbone that temporarily blocks self-assembly. The nvoc group is installed at the N-terminus of Cys, thus regulating both the isomerization and self-promoted oxidation.

While the nvoc group undergoes a Norrish type II reaction to form the N=O$_{nitroso}$ group **5**, the peptide performs an *S,N*-acyl rearrangement aligning the backbone and thus liberating the Cys-SH group, yielding Fmoc-ICA (**3a**$^\lambda$, Fig. 1)[25]. The N=O$_{nitroso}$ by-product **5** promotes the main reaction sequence, oxidizing the free thiol of Fmoc-ICA **3a**$^\lambda$ into its disulfide form DiFmoc-ICA **4a**$^\lambda$. We regulate the redox reversibility between **3a**$^\lambda$ and **4a**$^\lambda$ by introducing dithiothreitol (DTT) into the cascade, where the interconversion between both species is determined by the stoichiometry between N=O$_{nitroso}$ and DTT. The presence of both oxidation and reduction pathways therefore regulates the lifetime of **3a**$^\lambda$ and **4a**$^\lambda$ in solution, with the prevailing reaction defining the final species. To clarify the nomenclature, products formed within the cascade are denoted as **3a**$^\lambda$ for Fmoc-ICA and **4a**$^\lambda$ for DiFmoc-ICA, whereas the independently synthesized control
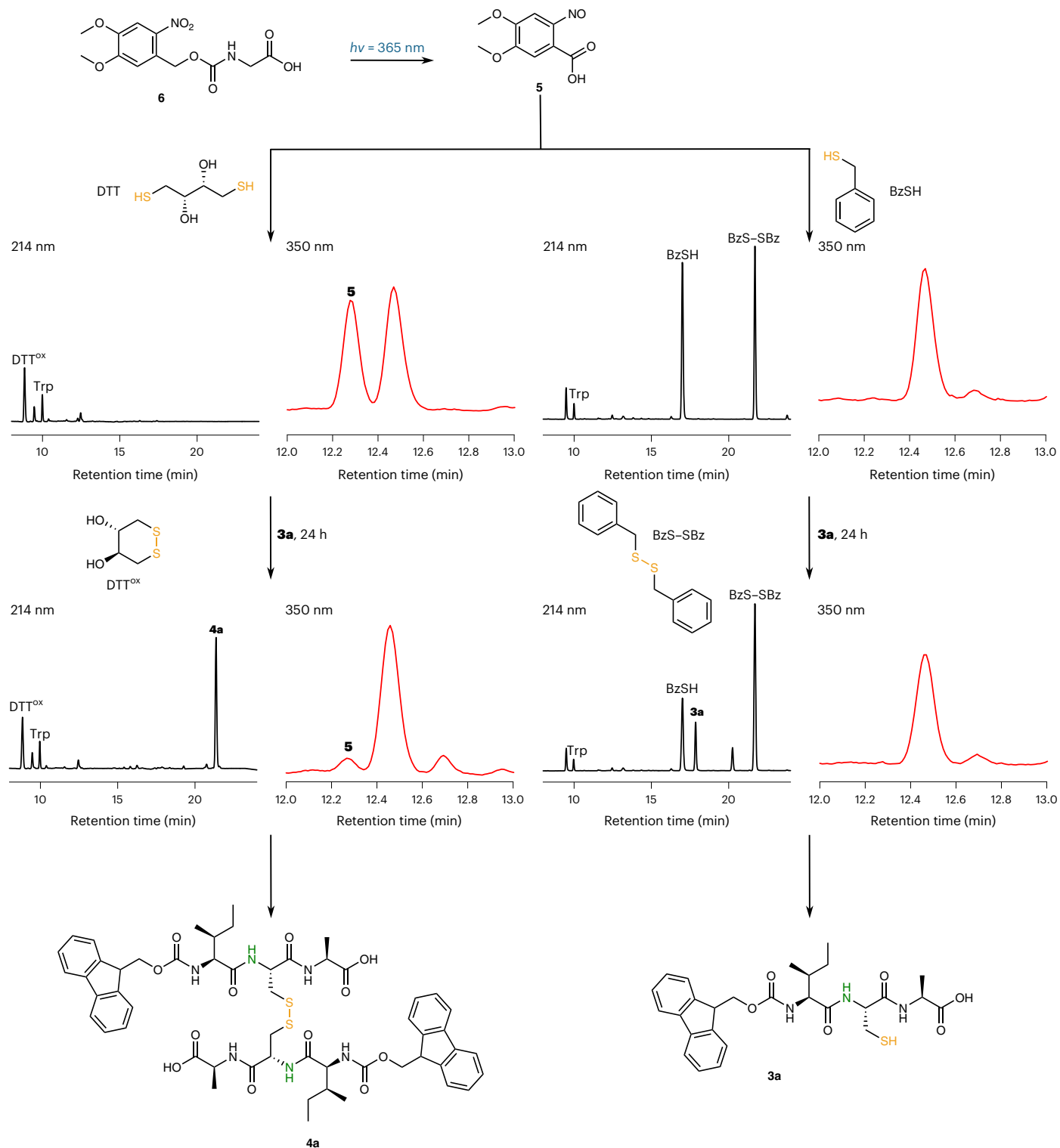
Fig. 4 | Decoupling the redox process by pretreating N=O_nitroso with different thiols. HPLC chromatograms of 6-nitroveratryl glycine (nvoc-Gly) **6** irradiated with 10 equiv. DTT (left) or BzSH (right) after 24 h. The intermediate N=O_nitroso **5** is consumed by BzSH to produce BzS–SBz, but is not consumed by DTT/DTT^ox.

Fmoc-ICA **3a** (1 equiv.) was then added and after a further 24 h samples were analysed by HPLC again. Oxidation into **4a** was observed for the DTT-pretreated reaction due to the presence of N=O_nitroso **5**. LC traces at 214 nm (black) and 350 nm (red) are shown for each step.

peptides are termed **3a** and **4a**, respectively. Structure formation is compared by (1) direct assembly where precursors are diluted in a poor solvent, (2) cascade assembly where **1a** is activated by light to eventually form the assemblies of **4a**$^\lambda$ and (3) cycled cascade assembly where DTT is added to interconvert **3a**$^\lambda$ and **4a**$^\lambda$ (Fig. 1). Hence, the control peptides and their cascade counterparts possess identical

chemical structures but differ in the way they are made available for assembly in solution.

Results and discussion

Peptide synthesis was carried out using Fmoc solid-phase peptide synthesis on Wang resin using *N,N′*-diisopropylcarbodiimide (DIC) and
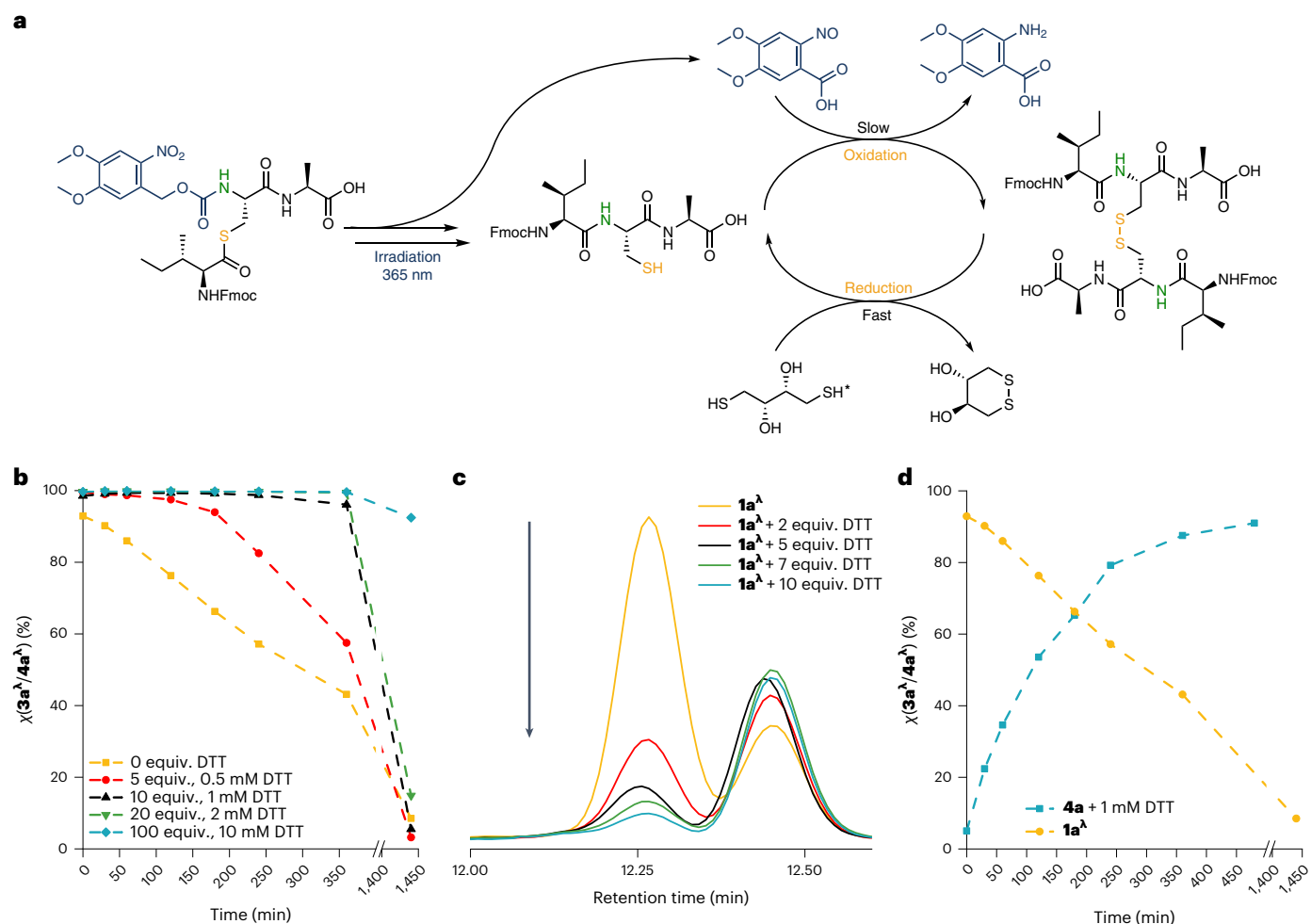
a

b

c

d

Fig. 5 | Modulation of the cascade by DTT. a, Reaction pathway of **1aλ** with DTT. N=O$_{nitroso}$ **5** and DTT form a redox cycle between **3aλ** and **4aλ** where they undergo multiple redox reactions. Denoted by DTT*, DTT also undergoes a separate, radical oxidation pathway with **5**. **b**, Molar proportion of **3aλ** versus **4aλ** with different concentrations of DTT over 24 h. **c**, HPLC chromatograms of **1aλ** with different concentrations of DTT. The peak of **5** is shown in the 350 nm trace. **d**, Molar proportion of **3aλ** versus **4aλ** for the reduction of 50 μM **4a** with 1 mM DTT and the cascade of 100 μM **1aλ** with 1 mM DTT over time. Note that 50 μM disulfide **4a** is equivalent to 100 μM of thiol **1aλ**.

ethyl (2Z)-2-cyano-2-(hydroxyimino)acetate (OxymaPure) for the iterative coupling steps (Fig. 2). To construct an isomerized Cys backbone, Fmoc-cysteine-monomethoxytrityl (Fmoc-Cys(Mmt)-OH) was used to enable orthogonal installation of the nvoc group via 6-nitroveratryl chloroformate on the N-terminus and Steglich esterification at the S-terminus. The so-called isopeptide was cleaved off from the resin with trifluoroacetic acid (TFA):triisopropyl silane (TIPS):H$_2$O (95:2.5:2.5) and purified by high-performance liquid chromatography (HPLC) to afford **1a**. As reference compounds, Fmoc-ICA **3a** and DiFmoc-ICA **4a** were synthesized using modified protocols (Supplementary Information). The serine analogue, where the cysteine of **1a** was substituted by serine to form **1b**, was also synthesized to elucidate the role of the thiol group in the oxidation reaction.

The molecular transformation of each step in the cascade was characterized by HPLC in methanol:NH$_4$HCO$_3$ buffer (1:1) at pH 7.4. This condition provides pH control and ensures that reaction intermediates and products remain in their molecular state and can therefore be quantified, using tryptophan as an internal standard. The optimum ultraviolet irradiation (365 nm) time of 180 s gave a deprotection conversion of 94% (Supplementary Fig. 20). Upon irradiation, the formation of each intermediate—the deprotected isopeptide **2aλ** and the S,N-rearranged peptide **3aλ**—and oxidation to the disulfide **4aλ** was monitored over 24 h (Fig. 3b). Separately synthesized **3a** and **4a** were used as references for

the retention times. Upon successful photodeprotection, the S,N-acyl shift to **3aλ** began immediately and proceeded with a t$_{1/2}$ (time required to attain 50% conversion) of 30 min. In comparison with the O,N-acyl shift[27] from **2bλ** to **3bλ** with t$_{1/2}$ > 6 h (Fig. 3c), the thiolate was demonstrated to be a better leaving group with an accelerated rearrangement kinetics. Although no further chemical changes were detected with the serine analogue **3bλ**, the cysteine derivative **3aλ** was further oxidized by the N=O$_{nitroso}$ into **4aλ** with a t$_{1/2}$ = 5 h (Fig. 3d). The control reference **3a** remains stable in its reduced form for 24 h under ambient conditions, confirming that its oxidation into **4aλ** was the result of the cascading step of the N=O$_{nitroso}$ by-product (Supplementary Fig. 25). We also studied the cascade reaction in an aprotic solvent, acetonitrile, in which the oxidation step of **3aλ** was delayed by more than a factor of 4 (t$_{1/2}$ > 24 h) (Supplementary Fig. 26).

The mechanism was investigated in parts by decoupling the cascade, separating the N=O$_{nitroso}$ production step and the thiol oxidation. Therefore, nvoc-glycine **6** was synthesized and, via irradiation, found to produce the N=O$_{nitroso}$ intermediate **5** (retention time, R$_T$ = 12.27 min) with quantitative conversion (Supplementary Fig. 33). In contrast to most findings that observed the nitrosobenzaldehyde to be the cleavage product, we found intermediate **5** to be the carboxylic acid derivative that was reported to form in oxygenated aqueous conditions (Supplementary Fig. 34)[28]. The addition of separately synthesized **3a**
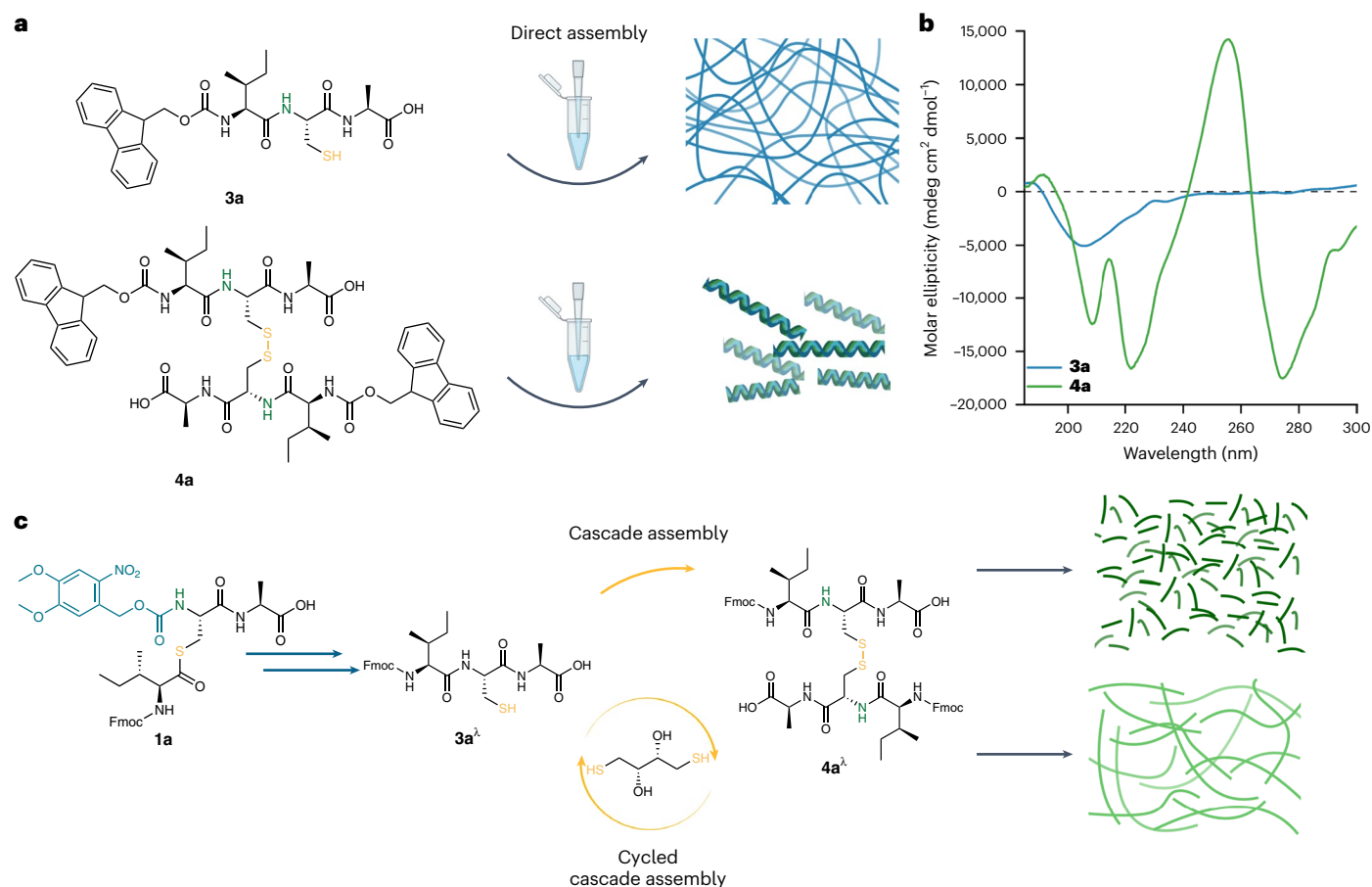
Fig. 6 | Influence of assembly pathways (direct, cascade, cycled cascade) on structure formation, chirality and long-range order. a, Direct assembly of **3a** and **4a**. **b**, CD spectra of **3a** and **4a** indicating distorted α-helical and atypical twisted β-sheet structures, respectively. **c**, Schematic of the cascade and cycled cascade assembly.

into the reaction successfully consumed the intermediate **5** to form **4a** (Supplementary Fig. 35). This reaction pathway was further confirmed by using benzyl mercaptan (BzSH, $R_T = 17.01$ min) as a substitute for **3a**, which resulted in the formation of the oxidized BzS–SBz ($R_T = 21.70$ min) (Supplementary Fig. 36). Each molecule of N=O$_{nitroso}$ **5**, apart from side reactions, is capable of oxidizing up to 4 equiv. of thiols[26].

From these findings, we postulate that the cascade from **1a$^\lambda$** to **4a$^\lambda$** can be modulated by interfering with the redox-sensitive species. As expected, complete inhibition of step **3a$^\lambda$** to **4a$^\lambda$** was observed by introduction of excess BzSH (10 equiv.), which reacted competitively with N=O$_{nitroso}$ **5** (Fig. 3f). Next, we further increase the complexity of the system by adding a selective reductant (DTT) into the cascade which reduces disulfide **4a$^\lambda$** back to thiol **3a$^\lambda$**. The coexistence of DTT and N=O$_{nitroso}$ **5** therefore forms a redox cycle, causing molecules of **3a$^\lambda$** and **4a$^\lambda$** to rapidly interconvert, with the prevailing stoichiometry and their kinetics determining the final redox state of the peptide at equilibrium. Hence, as long as DTT is present in solution, full oxidation by N=O$_{nitroso}$ **5** could not be achieved and would be observed as a net delay in the formation of **4a$^\lambda$** (Fig. 3e). Although DTT also possesses thiol groups, its intramolecular cyclization favoured an oxygen-promoted radical elimination from the N=O$_{nitroso}$ **5** core in the presence of water and oxygen[29,30]. The radical mechanism proposed would cycle the arylnitroso compound, which preserves the oxidation capacity of **5**. This was confirmed by treating N=O$_{nitroso}$ **5** with excess DTT (10 equiv.) for 24 h before adding 1 equiv. of thiol **3a** for a further 24 h incubation. The first 24 h of pretreatment, complete cyclization of DTT occurred, and in the following 24 h, complete oxidation of **3a** to **4a** showed the

activity of N=O$_{nitroso}$ **5** (Fig. 4). In contrast, pretreatment with excess BzSH (10 equiv.) completely consumed N=O$_{nitroso}$ **5** in the first phase, and hence no subsequent oxidation of **3a** was observed when added in the second phase (Fig. 4).

To understand the interplay of DTT and N=O$_{nitroso}$ in the redox cycle, we ran the full cascade over 24 h with varying amounts of DTT (5–100 equiv., 0.5 – 10 mM) and elucidated the reaction kinetics (Fig. 5a). By plotting the molar proportion of **3a$^\lambda$**/**4a$^\lambda$**, we observed a time-dependent suppression of the formation of disulfide **4a$^\lambda$** because the reduction by DTT initially dominated the reaction pathway and rapidly reduced **4a$^\lambda$** as soon as this was formed (Fig. 5b). Eventually, at lower DTT ratios, oxidation to **4a$^\lambda$** dominated as DTT supply decreased over time. Consequently, by increasing the amounts of DTT and thus the reduction rate, the delay in the formation of **4a$^\lambda$** was prolonged as long as sufficient N=O$_{nitroso}$ **5** was present (Fig. 5b,c). For example, at 1 mM of DTT, synthesized **4a** was reduced to **3a** with a $t_{1/2}$ = 2 h, whereas the DTT-free cascade oxidation into **4a$^\lambda$** by N=O$_{nitroso}$ **5** occured with $t_{1/2}$ = 5 h (Fig. 5d). Comparing these reaction rates at 1 mM DTT, the reduction by DTT controls the initial phase of the redox cycle, where **4a$^\lambda$** was only transiently present due to its rapid reconversion to **3a$^\lambda$**. Therefore, steady production of **4a$^\lambda$** could only occur when the rate of oxidation by N=O$_{nitroso}$ **5** began to dominate after 6 h (Fig. 5b).

Next, we studied the impact of the cascade pathway and redox cycling on structure formation through self-assembly at a standardized condition of methanol:NH$_4$HCO$_3$ buffer (1: 9) at pH 7.4. Reducing the organic solvent content to 1:9 (from 1:1 used in the reaction cycle in Fig. 3) was necessary to promote self-assembly. To confirm that the cascade proceeded efficiently under reduced amounts of methanol,
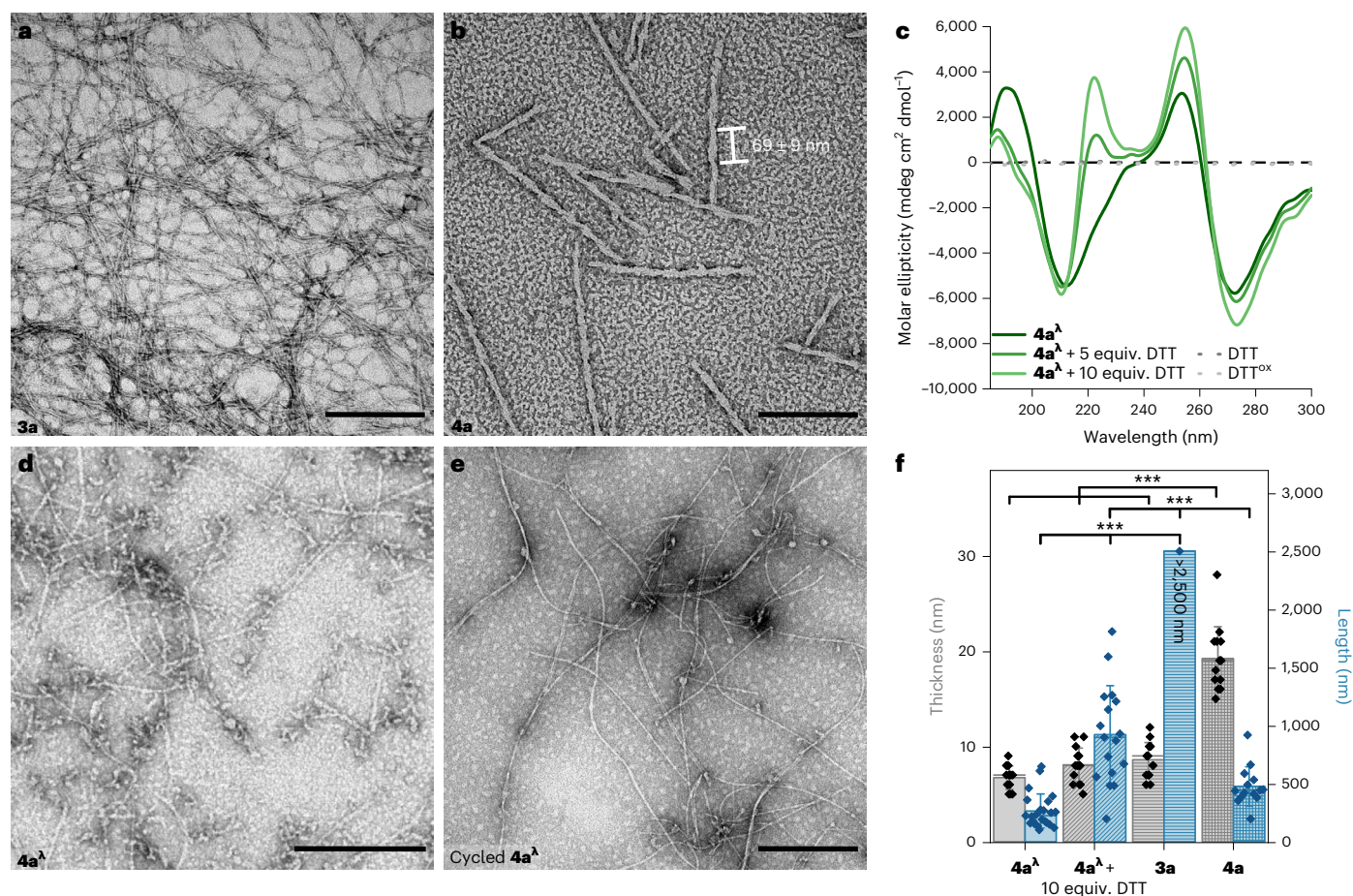
Fig. 7 | Influence of assembly pathways (direct, cascade, cycled cascade) on structure formation, chirality and long-range order. a, TEM image of **3a** revealing a network consisting of thin (9 ± 2 nm) fibres. **b**, TEM image of **4a** revealing twisted fibres with defined lengths (480 ± 170 nm) and periodicity (69 ± 9 nm). **c**, CD spectra of **4a^λ** with different equivalents of DTT indicating the emergence of secondary chirality at 222 nm and overall order as a function of redox cycling. DTT in its reduced and oxidized form (2 mM) as controls showed no contribution to the CD signature. **d**, TEM image of **4a^λ** showing fragmented fibres with average lengths of 260 ± 150 nm. **e**, TEM image of **4a^λ** with 10 equiv. DTT revealing the emergence of longer fibres (920 ± 420 nm). Scale bars in **a,b,d,e**, 250 nm. **f**, Thickness and length of the individual peptide fibres of monomers **3a**, **3a^λ**, **4a** and **4a^λ** obtained from TEM. Data are presented as mean ± s.d., $n = 14$. Statistical significance was calculated by analysis of variance with a Tukey post-hoc test: *$P < 0.05$, **$P < 0.01$, ***$P < 0.001$.

we performed a reverse analysis (by redissolving the assemblies in 50% methanol) and we showed that the conversion of **1a^λ** to **4a^λ** was complete at 24 h (Supplementary Fig 24). The critical assembly concentration (CAC) was determined by Proteostat assay, a general indicative fluorescence probe for peptide nanostructures (Supplementary Figs. 44–46)[31]. The control peptides **3a** and **4a** showed a CAC of 140 μM and 50 μM, respectively, whereas **4a^λ** showed a CAC of 30 μM. The higher fluorescence intensity produced by **4a** suggested that its superstructures contain higher molecular order than those of **3a**. By considering the findings of the CAC, we henceforth standardized the monomer concentrations to 200 μM, 24 h incubation time at room temperature for all subsequent structural studies to ensure that the formed superstructures are at equilibrium. Temperature-dependent ^{1}H NMR spectroscopy studies revealed that the assemblies of **3a** and **4a** (Supplementary Figs. 47 and 48) remained stable and did not depolymerize within 20–60 °C, taking into consideration the boiling point of methanol.

Circular dichroism (CD) spectroscopy analysis of **3a** and **4a** revealed major differences in the secondary structures of both assembled nanostructures. The control peptide **3a** showed a positive ellipticity at 187 nm and a negative Cotton effect at 205 nm attributed to the $n → π^*$ transitions of the peptide backbone typical of a distorted α-helical structure (Fig. 6b)[32]. Assemblies of **4a** exhibit different secondary structural features that are indicative of higher order.

Positive ellipticity at 191 nm and negative ellipticities at 208 nm and 222 nm indicated an atypical twisted β-sheet structure, corroborating the increased fluorescence detected by the Proteostat assay (Fig. 6b)[32]. Additionally, the characteristic $π → π^*$ transition of the Fmoc group at 255, 274 and 294 nm could only be found in the corresponding spectra of **4a**, indicating that the Fmoc group played a critical role in the emergence of supramolecular chirality during the assembly process. Having elucidated the supramolecular assembly characteristics by the direct assembly of **3a** and **4a**, we then studied how the reaction cascade would guide the assembly landscape. The reaction cascade to form monomer **4a^λ** affords self-assembled superstructures with combined secondary signatures of **3a** in the region <240 nm, and Fmoc interactions of **4a** in the region >240 nm. The possibility that the cascade did not drive to completion was excluded because post-assembly analyses by HPLC confirmed the total conversion of **4a^λ** and the absence of **3a^λ** (Supplementary Fig. 24). It is intriguing that **4a** and **4a^λ**, although molecularly identical, adopted different secondary structures within the same solvent. When the cascade was performed with redox cycling through DTT, the final superstructures revealed the emergence of a new positive ellipticity at 222 nm and an increase in the intensity of the Fmoc contribution at >240 nm (Fig. 7c). These observations increased in magnitude with increasing amounts of DTT.

Transmission electron microscopy (TEM) studies were conducted under the same conditions, that is, methanol:NH$_4$HCO$_3$ buffer (1:9) at pH 7.4 (Fig. 6), to investigate the morphologies of the formed supramolecular structures. TEM samples from the cascade were prepared, in situ, from the reaction mixture after 24 h, similar to the CD experiments. Each variation (for example, by DTT) was cross-checked via post-assembly HPLC analyses to ensure complete conversion to **4a**^{λ}. For the control peptides, direct assembly of **3a** resulted in the formation of a network consisting of thin (9 ± 2 nm) peptide fibres (Fig. 7a), whereas **4a** formed short and unusually defined fibres (Fig. 7b). Statistical analyses revealed that **4a** appears to have a critical length (480 ± 170 nm) with a twist periodicity of 69 ± 9 nm (Fig. 7f). Compared to **4a**^{λ} produced by the cascade, the resulting morphologies were largely fragmented fibres with a strong tendency to form localized clusters among few mature fibres (Fig. 7d). Without the irradiation step to initiate the reaction cycle, no assemblies were observed (Supplementary Fig 49). With redox cycling via DTT (10 equiv.), the delayed production of **4a**^{λ} showed a notable growth (>3-fold) in the length of the fibres (920 ± 420 nm) (Fig. 7e). In addition to the bulk analyses from CD, these TEM studies demonstrated that reaction pathways for the in situ generation of supramolecular assemblies can be used to modulate long-range structural order.

Conclusion

We have developed a reaction cascade that highlights the trademark structural plasticity in nature that enables different hierarchical states to be formed by one type of chemical identity. By merging reaction dynamics with a modulated global redox environment, a disulfide assembly precursor (**4a**^{λ}) has been found to exhibit different nanostructural orders, lengths and chirality. The disulfide bond is important in coordinating the aromatic contribution of the monomer towards structure propagation and the overall secondary structure of fibrils. Based on this principle, redox cycling between the thiol (**3a**^{λ}) and disulfide (**4a**^{λ}) results in the emergence of unique chiral signatures, ultimately forming different assembly states of **4a**^{λ}. The presented approach encompasses a number of strategies adopted in nature to regulate hierarchical structures through controlled and reversible production of assembly intermediates. We believe that this integrative chemical concept provides a fresh perspective on the bottom-up synthesis of nanostructures and expands the repertoire of dynamic supramolecular architectures that can be formed under mild conditions.

Methods

Light-induced *S,N*-acyl shift/*O,N*-acyl shift (HPLC)
The isopeptides were dissolved in 300 μl methanol (200 μM) and combined with 300 μl of an aqueous NH$_4$HCO$_3$ solution (5 mM, pH 7.4) to yield a 100 μM peptide solution. The peptide solutions were irradiated with ultraviolet light (365 nm) for 3 min while stirring at 300 r.p.m. and tryptophan (10 μM) was added as an internal standard. Aliquots of 10 μl were analysed at certain time points in an HPLC set-up. The kinetics were monitored for 24 h (**1a**) and 72 h (**1b**).

CD spectroscopy
For the measurement of the irradiated iso(Fmoc-I)nvocCA, the peptide was dissolved in 60 μl methanol (2 mM) and combined with 540 μl of an aqueous NH$_4$HCO$_3$ solution (5 mM, pH 7.4) to yield a 200 μM peptide solution. The solution was then irradiated with ultraviolet light (365 nm) for 10 min and incubated for 24 h. CD spectra were recorded at wavelengths from 300 to 185 nm with a bandwidth of 1 nm, data pitch of 0.2 nm and a scanning speed at 20 nm min^{-1} at 20 °C.

TEM
The isopeptide was dissolved in 60 μl methanol at a concentration of 2 mM and diluted with 540 μl NH$_4$HCO$_3$ buffer (5 mM, pH 7.4) to yield 100 μl solutions (200 μM). Then, the peptide was irradiated for 10 min

(365 nm) and 100 μl of this solution incubated for 24 h. TEM grids were prepared by pipetting 3 μl solution onto a Formvar-coated copper grid and incubating these for 5 min. After the incubation, the solutions were removed with filter paper, and the grids were stained with 7 μl 4% uranyl acetate solution for 5 min. The grids were washed three times with MilliQ water and dried before being measured.

Data availability

References

1. Westermann, S. & Weber, K. Post-translational modifications regulate microtubule function. *Nat. Rev. Mol. Cell Biol.* **4**, 938–947 (2003).
2. Gottschalk, A. C. & Hefti, M. M. The evolution of microtubule associated proteins—a reference proteomic perspective. *BMC Genomics* **23**, 266 (2022).
3. Bodakuntla, S., Jijumon, A. S., Villablanca, C., Gonzalez-Billault, C. & Janke, C. Microtubule-associated proteins: structuring the cytoskeleton. *Trends Cell Biol.* **29**, 804–819 (2019).
4. Schoenmakers, S. M. C. et al. Structure and dynamics of supramolecular polymers: wait and see. *ACS Macro Lett.* **11**, 711–715 (2022).
5. Schnitzer, T. et al. How subtle changes can make a difference: Reproducibility in complex supramolecular systems. *Angew. Chem. Int. Ed.* **61**, e202206738 (2022).
6. Rao, K. V. et al. Distinct pathways in 'thermally bisignate supramolecular polymerization': spectroscopic and computational studies. *J. Am. Chem. Soc.* **142**, 598–605 (2020).
7. Aida, T. et al. A rational strategy for the realization of chain-growth supramolecular polymerization. *Science* **347**, 646–651 (2015).
8. Lee, D. W., Kim, T., Park, I. S., Huang, Z. & Lee, M. Multivalent nanofibers of a controlled length: regulation of bacterial cell agglutination. *J. Am. Chem. Soc.* **134**, 14722–14725 (2012).
9. Weyandt, E. et al. Controlling the length of porphyrin supramolecular polymers via coupled equilibria and dilution-induced supramolecular polymerization. *Nat. Commun.* **13**, 248 (2022).
10. Robayo-Molina, I., Molina-Osorio, A. F., Guinane, L., Tofail, S. A. M. & Scanlon, M. D. Pathway complexity in supramolecular porphyrin self-assembly at an immiscible liquid–liquid interface. *J. Am. Chem. Soc.* **143**, 9060–9069 (2021).
11. Van Zee, N. J. et al. Potential enthalpic energy of water in oils exploited to control supramolecular structure. *Nature* **558**, 100–103 (2018).
12. Hou, L., Dueñas-Díez, M., Srivastava, R. & Pérez-Mercader, J. Flow chemistry controls self-assembly and cargo in Belousov–Zhabotinsky driven polymerization-induced self-assembly. *Commun. Chem.* **2**, 139 (2019).
13. Tantakitti, F. et al. Energy landscapes and functions of supramolecular systems. *Nature Mater* **15**, 469–476 (2016).
14. Aida, T., Meijer, E. W. & Stupp, S. I. Functional supramolecular polymers. *Science* **335**, 813–817 (2012).
15. Schnitzer, T., Jansen, S. A. H., Mabesoone, M. F. J., Vantomme, G. & Meijer, E. W. In situ synthesis of supramolecular polymers: finding the right conditions when combining covalent and non-covalent synthesis. *Angew. Chem. Int. Ed.* **61**, e202206729 (2022).
16. Rieß, B., Grötsch, R. K. & Boekhoven, J. The design of dissipative molecular assemblies driven by chemical reaction cycles. *Chem* **6**, 552–578 (2020).
17. Chen, Z. et al. Solvent-free autocatalytic supramolecular polymerization. *Nat. Mater.* **21**, 253–261 (2022).

18. Chakraborty, P. et al. Nanoengineered peptide-based antimicrobial conductive supramolecular biomaterial for cardiac tissue engineering. *Adv. Mater.* **33**, 2008715 (2021).

19. Álvarez, Z. et al. Bioactive scaffolds with enhanced supramolecular motion promote recovery from spinal cord injury. *Science* **374**, 848–856 (2021).

20. Yang, S. et al. Chemical fueling enables molecular complexification of self-replicators. *Angew. Chem. Int. Ed.* **60**, 11344–11349 (2021).

21. Mattia, E. & Otto, S. Supramolecular systems chemistry. *Nat. Nanotechnol.* **10**, 111–119 (2015).

22. Leira-Iglesias, J., Tassoni, A., Adachi, T., Stich, M. & Hermans, T. M. Oscillations, travelling fronts and patterns in a supramolecular system. *Nat. Nanotechnol.* **13**, 1021–1027 (2018).

23. Maiti, S., Fortunati, I., Ferrante, C., Scrimin, P. & Prins, L. J. Dissipative self-assembly of vesicular nanoreactors. *Nat. Chem.* **8**, 725–731 (2016).

24. Kueh, H. Y. & Mitchison, T. J. Structural plasticity in actin and tubulin polymer dynamics. *Science* **325**, 960–963 (2009).

25. Klán, P. et al. Photoremovable protecting groups in chemistry and biology: reaction mechanisms and efficacy. *Chem. Rev.* **113**, 119–191 (2013).

26. Ellis, M. K., Hill, S. & Foster, P. M. D. Reactions of nitrosonitrobenzenes with biological thiols: Identification and reactivity of glutathion-*S*-yl conjugates. *Chem. Biol. Interact.* **82**, 151–163 (1992).

27. Pieszka, M. et al. Controlled supramolecular assembly inside living cells by sequential multistaged chemical reactions. *J. Am. Chem. Soc.* **142**, 15780–15789 (2020).

28. Okamura, H., Iida, M., Kaneyama, Y. & Nagatsugi, F. *o*-Nitrobenzyl oxime ethers enable photoinduced cyclization reaction to provide phenanthridines under aqueous conditions. *Org. Lett.* **25**, 466–470 (2023).

29. Singh, S. P., Wishnok, J. S., Keshive, M., Deen, W. M. & Tannenbaum, S. R. The chemistry of the *S*-nitrosoglutathione/glutathione system. *Proc. Natl Acad. Sci. USA* **93**, 14428–14433 (1996).

30. Eyer, P. Reactions of oxidatively activated arylamines with thiols: reaction mechanisms and biologic implications. An overview. *Environ. Health Perspect.* **102**, 123–132 (1994).

31. Apicella, A. et al. Scaffold requirements for periodontal regeneration with enamel matrix derivative proteins. *Colloids Surf. B* **156**, 221–226 (2017).

32. Xing, Q. et al. Aromatic motifs dictate nanohelix handedness of tripeptides. *ACS Nano* **12**, 12305–12314 (2018).

Acknowledgements

Author contributions

P.R., D.Y.W.N. and T.W. conceived the project. P.R and R.M. performed the synthesis experiments and kinetics. P.R. conducted CD analysis and TEM with the advice of I.H., I.L. and K.L. R.M. and M.W. performed the NMR analysis. R.M. and P.R. performed the Proteostat assay. P.R., R.M., D.Y.W.N. and T.W. wrote the manuscript. D.Y.W.N. and T.W. supervised the project. All authors have read and approved the final manuscript.

Funding

Competing interests

The authors declare no competing interests.

Additional information

Supplementary information The online version contains supplementary material available at https://doi.org/10.1038/s44160-023-00343-1.

Correspondence and requests for materials should be addressed to David Y. W. Ng or Tanja Weil.

Peer review information *Nature Synthesis* thanks the anonymous reviewer(s) for their contribution to the peer review of this work.

Reprints and permissions information is available at www.nature.com/reprints.

Publisher's note Springer Nature remains neutral with regard to jurisdictional claims in published maps and institutional affiliations.